Teffs, J, Mazzali, PA, Medler, K and Hachinger, S

 A massive, energetic model for the luminous transitional Type Ib/IIb SN 2020cpg

http://researchonline.ljmu.ac.uk/id/eprint/18120/

Article

For more information please contact researchonline@ljmu.ac.uk

A massive, energetic model for the luminous transitional Type Ib/IIb SN 2020cpg

J. Teffs [ID],[1][*] P. A. Mazzali,[2,3] K. Medler [ID][2] and S. Hachinger[4]

[1]*Areté Associates, 3194 N Swan Rd, Tucson, AZ 85712, USA*
[2]*Astrophysics Research Institute, Liverpool John Moores University, IC2, Liverpool Science Park, 146 Brownlow Hill, Liverpool L3 5RF, UK*
[3]*Max-Planck Institut für Astrophysik, Karl-Schwarzschild-Str 1, D-85741 Garching, Germany*
[4]*Leibniz Supercomputing Centre (LRZ), Boltzmannstr. 1, D-85748 Garching, Germany*

ABSTRACT

Using a combined spectral and light-curve modelling approach, we fit a massive and energetic explosion model to the luminous Type Ib/IIb SN 2020cpg. This model has an ejected mass of $\sim(7 \pm 2)\,M_\odot$ with a final explosion energy of $\sim(6 \pm 1) \times 10^{51}$ erg with $M_{\mathrm{Ni}} = 0.27 \pm 0.05\,M_\odot$. The early spectra are hot and blue with weak He I lines, and a complicated Hα region suggested to be a multicomponent feature. Modelling the spectra required $\sim 0.08\,M_\odot$ of H at velocities $> 11\,000\,\mathrm{km\,s^{-1}}$ and a total He mass of $\sim 1.0\,M_\odot$ at velocities $> 9500\,\mathrm{km\,s^{-1}}$ above CO-rich ejecta. This model has a ratio of kinetic energy and ejected mass of $0.85^{+0.5}_{-0.3}$ foe $M_\odot{}^{-1}$. The high luminosity and explosion energy results in a broadened Hα line that is blended with Si II, C II, and He I, which led to the initial classification of SN 2020cpg as a Type Ib. We instead classify SN 2020cpg as a bright transitional event between the Type Ib and Type IIb classes. Comparing our model parameters to stellar evolution models, a progenitor mass of 25–30 $M_\odot$, i.e. stripped of most of the hydrogen shell and of some of the helium shell prior to collapse produces a He core of comparable mass. The excess ^{56}Ni production in SN 2020cpg as compared to objects of similar ejected mass may suggest evidence of additional energy sources such as a failed GRB or weak magnetar energy injection, or a smaller remnant mass.

Key words: radiative transfer – supernovae: general – supernovae: individual: SN2020cpg.

1 INTRODUCTION

Stripped Envelope Supernovae (SE-SNe) are a class of supernovae in which some fraction of the H/He in the outer layers of the progenitor star is lost prior to collapse. SNe Type IIb have progenitors that are He-rich, but H-poor compared to other SNe Type II while SNe Type Ib also have He-rich progenitors but show weak or no H lines in their spectra. Mechanisms such as periods of high-mass loss driven by stellar winds (e.g. Nomoto, Iwamoto & Suzuki 1995; Langer 2012) or binary interaction (e.g. Nomoto et al. 1995; Yoon, Woosley & Langer 2010) have been explored as ways to produce these SE-SNe with varying degrees of success. Some SNe Type Ic are thought to show signs of He in the spectra (e.g. SN 1994I Sauer et al. 2006) and some SNe Type Ib show signs of Hα (e.g. SN 2007Y Stritzinger et al. 2009).

SN 2020cpg was first detected on 2020 February 15 (Nordin et al. 2020) (MJD = 58894.52) with a last non-detection nine days prior. SN 2020cpg was classified as a Type Ib, five days after initial detection (Amenouche et al. 2020; Poidevin et al. 2020). The classification spectrum showed weak features, a very blue colour, and a spectral feature that could be Hα while the later spectra showed evidence of a persistent Hα-like feature. Medler et al. (2021) suggest that SN 2020cpg contains a two component Hα region with both a low- and a high-velocity feature that either combine in later

epochs or the high-velocity Hα weakens. The bolometric luminosity of SN 2020cpg peaks at $\sim 6.0 \times 10^{42}$ erg s^{-1}, placing SN 2020cpg on the luminous end of the observed Type Ib/IIb distribution. Using two approximation methods, Medler et al. (2021) estimates a final ejected mass between 3 and 5 $M_\odot$ of material at a final kinetic energy between 3 and 9×10^{51} erg with a synthesized mass of 0.27 $M_\odot$ of ^{56}Ni. Compared to the studies of other SNe Type IIb (e.g. Lyman et al. 2016; Prentice et al. 2016; Taddia et al. 2018), the estimated explosion properties of SN 2020cpg are higher than average.

The abundance tomography method Stehle et al. (2005) has been used to model the abundance stratification of Type Ia (e.g. Hachinger et al. 2012b; Mazzali et al. 2015; Ashall et al. 2016) and Type Ic (e.g. Mazzali et al. 2006; Sauer et al. 2006; Mazzali et al. 2017; Teffs et al. 2021). To date, only one Type IIb SN (SN 2003bg) has been modelled using this method with SN 2008ax being approximately modelled in Hachinger et al. (2012a). SN 2003bg was an energetic broad-lined SN Type IIb (Mazzali et al. 2009) with an ejected mass, or M_{ej}, of $\approx 4\,M_\odot$, a final explosion energy, or E_{k}, of ≈ 5 foe, and a thin hydrogen-rich shell of 0.05 $M_\odot$ above a v_{ph} of 9000 km s^{-1}. The early broad spectral phase of SN 2003bg as well as the high E_{k} led to its identification as a hypernova. Hachinger et al. (2012a) reproduced the observed spectra of SN 2003bg with a 4.7 $M_\odot$ model at a final $E_{\mathrm{k}} \approx 1$ foe. This was not a complete model, but did match other estimates of model properties (Taubenberger et al. 2011).

For SN 2003bg, to properly model the H/He features, a 'non-thermal factor' (e.g. Harkness et al. 1987) was used to artificially increase the level of populations in order to match the observed

[*] E-mail: jacobteffs@gmail.com

Table 1. The dates of the modelled spectrum. The estimated explosion date is MJD = 58887.7 ± 2.1, but a t_{exp} of MJD = 58886 best reproduces the spectral evolution.

MJD	Phase (t_p) [d]	Phase (t_{exp} (obs)) [d]	Phase (t_{exp} (Model)) [d]
58898.16	− 4.1	10.46	12.5
58899.36	− 2.9	11.66	13.2
58903.61	1.3	15.91	17.5
58908.00	5.7	20.30	21.6
58911.23	8.9	23.50	24.8
58917.60	14.7	29.90	31.2

Table 2. A summary of explosion properties derived using the spectral modelling in this work compared to estimate was found in Medler et al. (2021), which includes a fit using Arnett's method (Arnett 1982) and a fit by re-scaling light curves based on Mazzali et al. (2013).

Method	Mass [M$_\odot$]	M_{Ni} [M$_\odot$]	E_k [10^{51} erg]
Arnett fit	3.4 ± 1.0	0.27 ± 0.08	2.9 ± 0.9
Re-scaled light curves	5.5 ± 2	0.3 ± 0.1	∼9 ± 3
Spectral modelling	7 ± 2	0.27 ± 0.05	6 ± 1

line strengths not reproduced in the nebular approximation. For SN 2008ax however, a NLTE calculation for H/He was used to determine the excitation and ionization of H/He, matching the line strengths and broadness of the observed H/He spectral lines without artificially increasing the level populations. For the spectral modelling of SN 2020cpg, we include the non-thermal effects on hydrogen and helium using the module developed in Hachinger et al. (2012a) in order to best reproduce the observed H/He lines, and makes SN 2020cpg the first Type IIb to be modelled using this set-up.

In this work, we use the abundance tomography method to model the photospheric spectra of SN 2020cpg to produce a consistent model and use the density profile to produce a bolometric light curve. In Section 2, we discuss the data selected for the modelling process and any relative observational information. In Section 3, we present and discuss the consistent model for the light curve and the photospheric phase of the spectral evolution. We discuss and analyse the properties of our model for SN 2020cpg in Section 4.

2 DATA

A companion paper by Medler et al. (2021) describes the data collection, reduction, and observational analysis for SN 2020cpg. A few important observational details are repeated here. We adopt the same redshift ($z = 0.037$), distance modulus (36.05 ± 0.15 mag), the bolometric light curve as calculated in Medler et al. (2021), and adopt the same explosion date of MJD = 58887.7 ± 2.1 d as a first approximation.

In total, we select seven spectra from $t_p - 4.2$ d to $t_p + 22.7$ d, where t_p is the time of the maximum bolometric luminosity. The earliest available spectrum is too noisy to discern any features and is not modelled. Table 1 shows the epochs of the modelled spectra, both with respect to the new explosion date, t_{exp}, and t_p. The early phases show incomplete photometric coverage, which makes proper flux calibration in these phases challenging. This may result in a mismatch in the flux during the modelling phase, and can show a mismatch in the red and blue wavelengths of the spectral model. In particular, the lack of near-UV limits a proper calibration in the early phases. As such, the error in flux calibration can be 5–15 per cent.

3 MODELLING

To model SN 2020cpg, we follow the abundance tomography method which has been used to model the broad-lined Type IIb SN 2003bg (Mazzali et al. 2009), the broad-lined Type Ib SN 2008D (Mazzali et al. 2008), and the narrow lined Type Ic SN 2017ein (Teffs et al. 2021). This method allows for the estimation of the explosion energy (E_k), the ejected mass (M_{ej}), the ^{56}Ni mass (M_{Ni}), and the distribution of elements that produce strong optical lines as a function of

photospheric velocity (v_{ph}). The addition of nebular phase modelling can further improve the estimate of the mass (see Ashall & Mazzali 2020), but no nebular spectra were taken for SN 2020cpg. By also modelling the light curve, the degeneracy involved in the M_{ej} and E_k inherent to approximate methods, like Arnett's method (Arnett 1982), can be separated. Medler et al. (2021) estimates the M_{ej}, E_k, M_{Ni}, and t_{exp} for SN 2020cpg, which for this work are used as first approximations. These values, as well as those found from the modelling, are summarized briefly in Table 2.

To model the light curve, we first adopt a density profile from Teffs et al. (2020) that represents a 22 M$_\odot$ progenitor stripped of nearly all of its hydrogen with a final ejected mass of 5.8 M$_\odot$. This model contains 1.3 M$_\odot$ of He and 0.1 M$_\odot$ of H above a ∼4.4 M$_\odot$ of CO-rich material and was exploded to a final $E_k = 3$ foe. The initial abundance profile is also taken from this model. This model is selected as a starting point as its late time synthetic spectra (see Teffs et al. 2020) showing strong similarities to the late time of SN 2020cpg with respect to line velocity and width, suggesting it's abundance distribution is a reasonable first approximation. Using this density profile, we model the light curve using a code described in Cappellaro et al. (1997), Mazzali et al. (2001), which calculates the emission and propagation of the γ-rays and positrons produced by the decay of ^{56}Ni, and subsequently ^{56}Co, into the homologously expanding ejecta using a Monte Carlo method. The deposited energy from the decay is recycled into optical photons and the resulting propagation is also followed using a similar Monte Carlo scheme. We adopt gamma-ray and positron opacities of $\kappa_\gamma = 0.027$ cm^2 g^{-1} and $\kappa_{e^+} = 7$ cm^2 g^{-1} (Axelrod 1980). The optical opacity is both time and metallicity dependent, which aims to reproduce the dominance of line opacity in the ejecta (Mazzali et al. 2001; Ashall et al. 2019). The synthetic light curve is compared to the observed pseudo-bolometric light curve, and the M_{ej}, E_k, and the mass and distribution of ^{56}Ni are modified until an approximate fit is achieved. These parameters are modified by rescaling the density profile using the uniform scaling relations as used in Hachinger et al. (2009), Teffs et al. (2021).

Once a synthetic bolometric light curve roughly matches the observed bolometric light curve, we use the resulting density profile and associated ^{56}Ni abundance distribution in our Monte Carlo radiative transfer code with our NLTE module, described in detail in Mazzali & Lucy (1993), Lucy (1999), Mazzali (2000), Hachinger et al. (2012a). For each of the chosen spectra, the photospheric luminosity and velocity, L_{ph} and v_{ph}, respectively, are systematically changed until the rough spectral shape and flux level are found to reproduce the observed spectrum. As discussed in Ashall & Mazzali (2020), once a suitable pair of v_{ph} and L_{ph} are found, these values can change by 5–10 per cent in either direction before the fit begins to suffer visibly. The elemental abundances are modified until the velocity and strength of each feature is reasonably reproduced, and this process is iterated from the earliest modelled spectrum until the last modelled spectrum. Once a suitable spectral fit is found, the final

density and abundance profile is used in the light-curve code again to produce a final synthetic bolometric light curve as a final check.

Using these methods, we arrive at a model with an $M_{ej} = 7 \pm 2\,M_\odot$, a ^{56}Ni mass of $0.27 \pm 0.05\,M_\odot$, and an $E_k = 6 \pm 1$ foe. These values and the approximations from Medler et al. (2021) are given in Table 2, and show reasonable agreement between the approximate methods.

3.1 Spectral model

Fig. 1 shows the observed spectra at the six chosen epochs compared to our modelled synthetic spectra. The abundance profile derived from spectral modelling is compiled in Fig. 2. As mentioned previously with no nebular spectra, we are unable to constrain the abundances of the material below the last modelled photosphere of ~ 8000 km s^{-1}, and assume a constant abundance profile from the last modelled epoch. As the H/He shell is above this photosphere, this does not change the total H/He mass estimated.

3.1.1 $t_p - 4.1$ d, $t_{exp} + 12.5$ d, 2020 February 19

The first modelled epoch (panel (a) in Fig. 1) is the second earliest spectrum, but shows a good signal-to-noise (S/N) ratio with only a few days difference in phase. This synthetic spectrum is modelled with $v_{ph} = 13\,000$ km s^{-1} and $\log(L_{ph}) = 42.64$ [erg s^{-1}]. The observed spectrum is hot and blue with only a few strong features such as the primary optical He I line at 5875 Å. For this modelled spectrum, we include an abundance of less than 1 per cent for S, which produces a set of S II lines in the 4500–5500 Å region, reducing the average flux in this region, without producing significant lines. We include a low percentage of Fe-group element but the high temperature due to the required luminosity results in strong ionization, and does not produce the commonly observed Fe II lines. We also note that the synthetic spectrum peaks near ~ 3500 Å, which is beyond the observed spectrum. In this model, the high-velocity Hα predicted by Medler et al. (2021) is identified as a Si II line, while the broad Hα region is comprised of C II, Hα, and He I. This feature is discussed in detail in Section 4.1.

3.1.2 $t_p - 2.9$ d, $t_{exp} + 13.2$ d, 2020 February 20

The second modelled spectrum (panel (b) in Fig. 1) has a wider observed wavelength range and is modelled with $\log(L_{ph}) = 42.69$ [erg s^{-1}] and $v_{ph} = 12\,500$ km s^{-1}. At only 1.2 d after the previous epoch, the observed spectrum and synthetic model shows a few changes beyond an improved S/N. The previous epoch showed the synthetic spectrum peaking near 3500 Å, and in this later spectrum the wavelength coverage extends further in the near-UV showing that the observed spectrum does peak near 3500 Å. This matches the prediction in the previous epoch that the early phases of SN 2020cpg are hot and blue. The He I features in the synthetic spectra do not quite match the observed spectrum, showing slightly weaker absorptions. This may be due to the overall flux level, either in the synthetic spectrum or in the flux calibration. In particular, the blue region of the modelled spectrum is lower in flux while the redder portion of the spectrum is higher in flux than the observed spectrum. This may be due to too much Fe-Group elements blocking too much near UV flux and re-emitting in the red. Reducing the Fe-group abundances worsens the overall fit of this epoch and several others, suggesting that the mismatch may be due to a mismatch in flux calibration. Beyond this, the rest of the spectrum is largely well reproduced
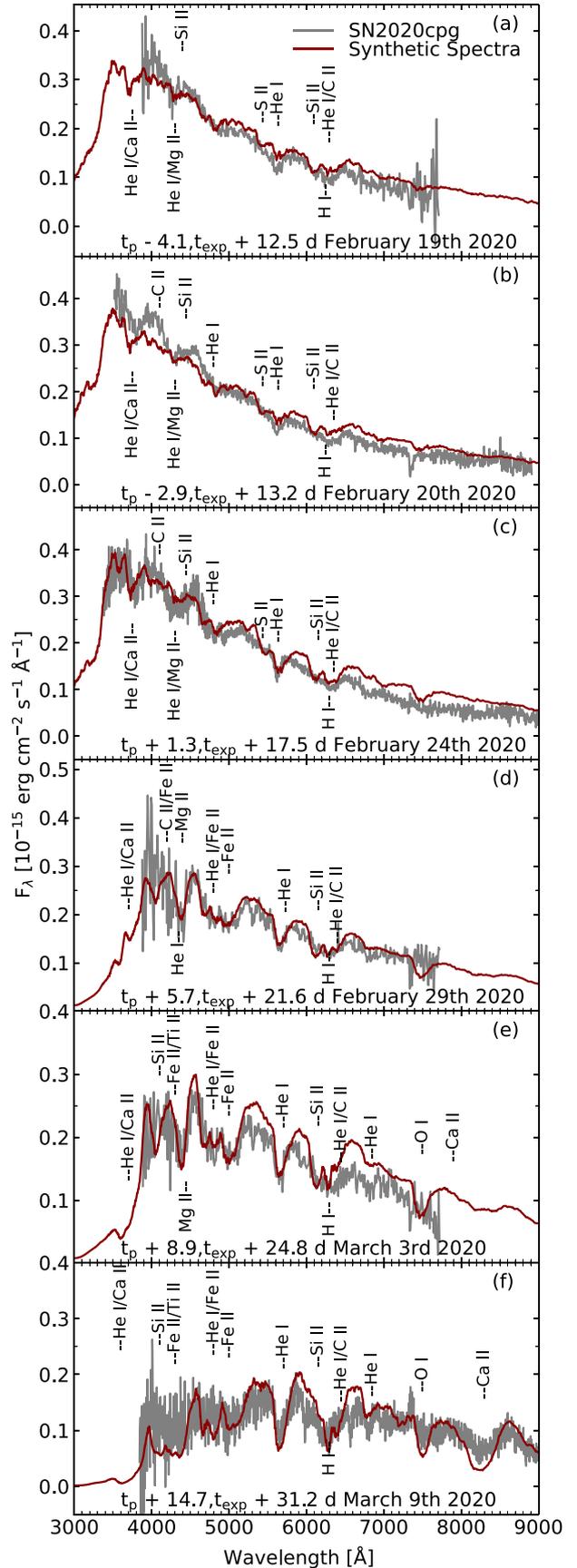
Figure 1. Synthetic spectral and observed spectra for 6 epochs of SN 2020cpg covering 20 days of spectral evolution. The commonly observed and strongest lines are identified in the spectra.
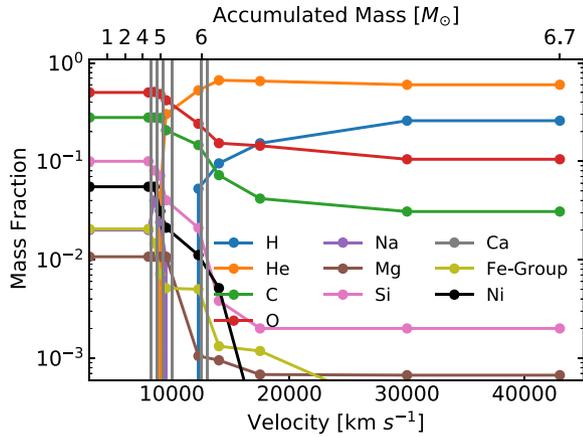
Figure 2. Abundance profile for the synthetic model in Fig. 1. The vertical grey lines are the locations of the photospheres in Fig. 1. Fe-group is a combined selection of elements, such as Fe, Ti, V, Mn, and Cr. The composition below the v_{ph} of 8000 km s^{-1} is extended to the inner boundary of the scaled model at 3000 km s^{-1}, and the composition of this material is assumed to be constant from the last modelled epoch. Material is likely to extend below 3000 km s^{-1}, but the lack of nebular spectra prevents strong constraints on the innermost density and abundance profile.

3.1.3 $t_p + 1.3$ d, $t_{exp} + 17.5$ d, 2020 February 24

The third modelled spectrum (panel (c) in Fig. 1) has $\log(L_{ph})$ = 42.69 [erg s^{-1}] and v_{ph} = 10 000 km s^{-1}. At the photosphere for this epoch, the abundance of H is reduced to zero and the He abundance is also reduced to ~50 per cent of the total abundance. This matches the line velocity estimates (Medler et al. 2021) that shows the Hα flattening out ~10 000 km s^{-1}, suggesting this is the lower boundary of the H-rich region. As in the previous epoch, we see a slight increase in flux in the 7000–9000 Å region despite the rest of the flux level matching the observed reasonably well. Additionally, the Fe II lines are beginning to develop, while the S II line is starting to weaken as the ejecta continue to expand and cool.

3.1.4 $t_p + 5.7$ d, $t_{exp} + 17.5$ d, 2020 February 29

The synthetic spectrum in panel (d) in Fig. 1 has $\log(L_{ph})$ = 42.61 [erg s^{-1}] and v_{ph} = 9250 km s^{-1}. At this epoch, the slope of the spectrum has begun to flatten and the peak has moved to redder wavelengths. As the ejecta cool, the C II lines begin to weaken as C is less ionized while the slow accumulation of Fe in the ejecta has produced the commonly observed $\lambda\lambda\lambda$ 4924, 5018, 5169 Fe II lines. The 6000–6500 Å region has developed a 'w-shaped' feature with the strongest contributors being Si II, Hα, and He I from blue to red. In previous epochs, this feature was blended with a strong C II contribution. The λ5875 He I line is well reproduced as are the weaker λ6678 and λ7065 lines.

3.1.5 $t_p + 8.9$ d, $t_{exp} + 23.5$ d, 2020 March 3

The synthetic spectrum in panel (e) in Fig. 1 has $\log(L_{ph})$ = 42.56 [erg s^{-1}] and v_{ph} = 8750 km s^{-1}. The majority of the features are well reproduced with a few minor exceptions. The Si II line at 4000 Å, with weaker contributions from H/He lines, is too dominant in our models, despite this being needed to best reproduce the 6500 Å region. The Hα line is somewhat narrow in this epoch despite the broad and blended region.
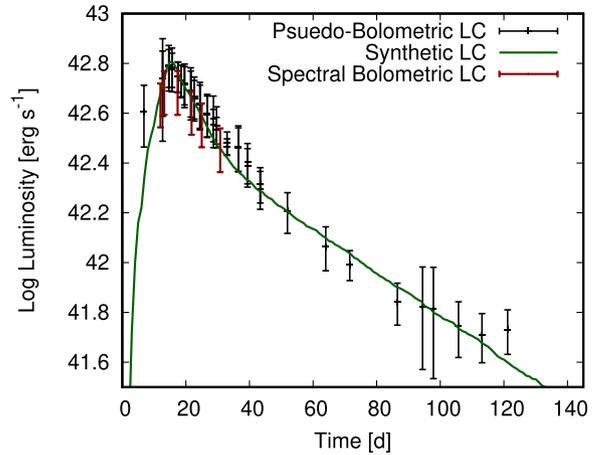

Figure 3. The pseudo-bolometric light curve as calculated from the observations (in black) compared to the synthetic light-curve code (in green), and the outputted bolometric luminosity as calculated from the spectral synthesis code (in red). We include a 10 per cent error bar for the spectral synthesis code as discussed in Section 3.

3.1.6 $t_p + 14.7$ d, $t_{exp} + 29.9$ d, 2020 March 9

The synthetic spectrum in panel (f) in Fig. 1 has modelled parameters of $\log(L_{ph})$ = 42.46 [erg s^{-1}] and v_{ph} = 8250 km s^{-1}. At this epoch, the location of the photosphere becomes harder to define strictly as nebular emission contributions are becoming non-negligible. This spectrum has a low-S/N ratio, but most features are well reproduced in the model. The photosphere by this phase has receded into the CO core and most features are unlikely to change until the evolution approaches the nebular phase. The NIR Ca II triplet is well reproduced in velocity, but slightly too strong. The blue wing of the 6500 Å region is not so well reproduced, which could suggest more hydrogen or silicon would be needed at higher velocities to broaden this feature.

3.2 Light-curve model

Fig. 3 shows three light curves; the pseudo-bolometric light curve from Medler et al. (2021), the light curve as calculated from the light-curve code based on the abundance and density profiles obtained from the spectral modelling, and the bolometric luminosity (L_{Bol}) from the spectral synthesis code. The error from the pseudo-bolometric light curve is fairly significant, but both the light-curve code and the spectral synthesis code produce luminosities within the error bounds. The overall shape of the synthetic light curve matches the shape and behaviour of the observed light curve with a few minor deviations. The largest deviation is that of the earliest photometric point. Increasing the ^{56}Ni mass or mixing ^{56}Ni to higher velocities may match this early photometric point, but this data point is only constrained by a pair of r' and g'-band data points. The late time bolometric light curve (t > 80 d) also deviates slightly from the synthetic light curve, but the scatter in the data is fairly large and our light curve does match the overall trend of the late time light curve.

The light curve as calculated from the six spectral epochs also reproduces the light curve in the 20 days around t_p. An estimated 10 per cent error is included as the luminosity can likely shift of 5–10 per cent before the fit suffers significantly (e.g. Ashall & Mazzali 2020). These points are slightly underluminous compared to the previous synthetic light curve and calculated light curve, but still fall within error bounds while also reproducing the spectra adequately.

4 DISCUSSION

4.1 Hydrogen identification

Medler et al. (2021) suggest a two component Hα feature, consisting of a weak, high-velocity line (v ∼ 16 000–21 000 km s^{-1} in the earliest epochs) and a lower velocity line at 13 000 km s^{-1} is responsible for the 6500 Å region. The high-velocity line eventually weakens, or merges with the lower velocity line, as the photosphere recedes into the ejecta with a high-velocity detached H shell suggested as the explanation. From the spectral analysis in this work, we do not need a detached H shell to reproduce the spectral evolution of SN 2020cpg. Instead, a model with ∼0.08 M$_\odot$ above a v_{ph} 11 000 km s^{-1} and a mixture of other elements can reproduce the shape, strength, and evolution of the Hα feature.

In our best-fitting model, a combination of Si II, Hα, He I, and C II lines reproduce this region in both the early epochs and late time epochs as shown in Fig. 1. The abundances of carbon above the first modelled epoch at $v_{ph} = 12\,500$ km s^{-1} is 5 per cent of the total abundances with a slightly weaker contribution from silicon. Comparing this abundance to the pre-explosion abundance profiles for the models in Teffs et al. (2020), the carbon abundance in the unmixed models is roughly 1 per cent in the H-rich shell in the IIb-like models and closer to 5 per cent in the He-rich shell in the Type Ib models. In our model for SN 2020cpg, we do not have a shell where the H is dominant, and instead have a mixed He-rich region, suggesting that the presence of C at 5 per cent in this region is a reasonable assumption.

Due to the high luminosity of SN 2020cpg, the ionization regime of the available material is much higher than comparable Type Ib/IIb events. The high temperature in the early phases ionizes the majority of the carbon to C II, resulting in the strong C II lines near 6500 Å. As the ejecta cool and expand, the carbon shows less ionization and contributes less to the feature while the He I feature becomes more dominant. In the early phases, H/He only contribute weakly to the feature as both are almost entirely ionized. Si is doubly ionized and is only single ionized at high velocities in the early phases, resulting in a high-velocity Si II feature, likely identified as the detached shell. In the later phases, H/He and Si show less ionization with an increase in Hα and He I line strengths due to an increase in the deposition of γ-rays and positrons, while Si II increases in strength as the abundance of Si increases in the CO rich inner material.

In order to test if the model requires hydrogen to match the behaviour and evolution of the ∼6500 Å region, we transfer the abundance of hydrogen in our best-fitting model into the helium abundance. This is an acceptable approximation as the hydrogen is only present where the helium resides. There is only a slight flux difference in the first modelled spectrum in Panel (a) of Fig. 4. In the next two epochs, (Panels (b) and (c) in Fig. 4), the 6500 Å region splits into two features without hydrogen present in the model; the Si II feature at 6100 Å and a He I/C II feature near 6500 Å.

4.2 Classification as a Type Ib or IIb?

As discussed, SN 2020cpg was initially classified as a Type Ib, before a later re-classification of Type IIb. While some SNe Type Ib have shown the presence of a Hα line, the line is often transient or hard to clearly define, while SNe Type IIb typically shows a strong Hα line and some evidence of the other Balmer series lines. SN 2020cpg shows no evidence of the Balmer series lines besides Hα, but the Hα is not easy to separate from the features nearby, making identification difficult. However, our model does require hydrogen in order to
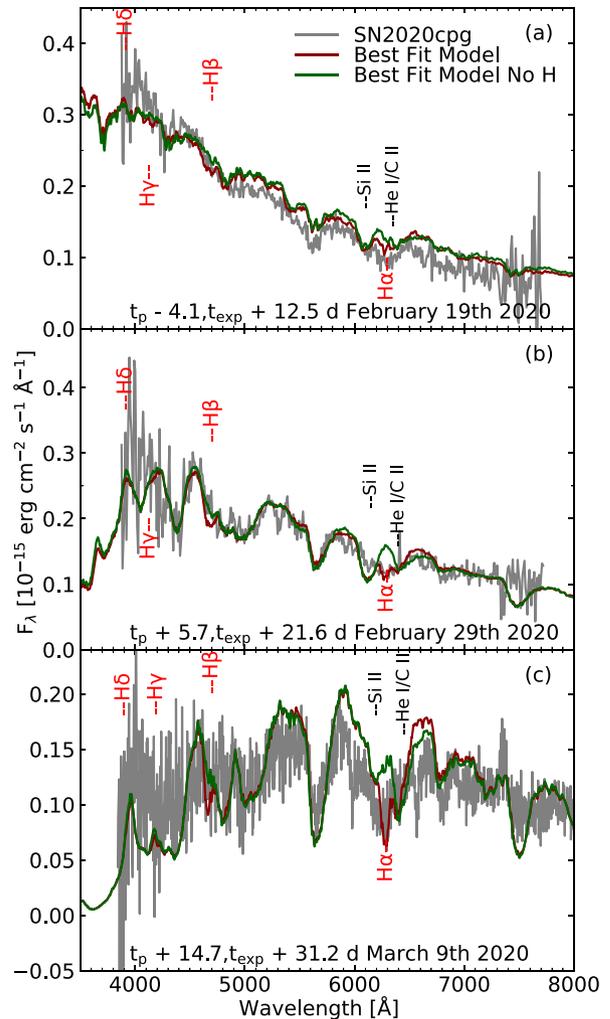

Figure 4. Three selected epochs compared to two spectral models; the best-fitting model from Fig. 1 (red), and a model where the H in the abundance profile is replaced by He (in green).

reproduce the spectral evolution. As such, the SN 2020cpg is best identified as an odd, luminous SNe that is between the Type Ib/IIb classes, similar to the conclusion of Medler et al. (2021).

Using the physical classification system (e.g. Prentice & Mazzali 2017), SN 2020cpg always fits in between two new classes. Both SNe Type IIb (I) and Type Ib (II) in this system show a weak Hα line, similar to SN 2020cpg, and are separated by the equivalent width. The Hα line is blended with other features preventing an accurate measurement. In this classification system, SN 2020cpg falls between the Type IIb (I) and Type Ib (II) classes.

4.3 Explosion properties

Several groups have estimated explosion properties for samples of SNe Type Ib/IIb, and these are summarized in Table 3 for simplicity. These studies use a semi-analytic approach in estimating the SNe Type Ib/IIb explosion properties and often use differing assumptions for the opacity making direct comparisons challenging. The average estimates for M_{ej} and M_{Ni} from Prentice et al. (2019) are much lower than the modelled explosion properties for SN 2020cpg. This also holds true for the parameter estimates in Lyman et al. (2016). Taddia

Table 3. A sample of Type Ib/IIb model properties taken from several recent sample studies.

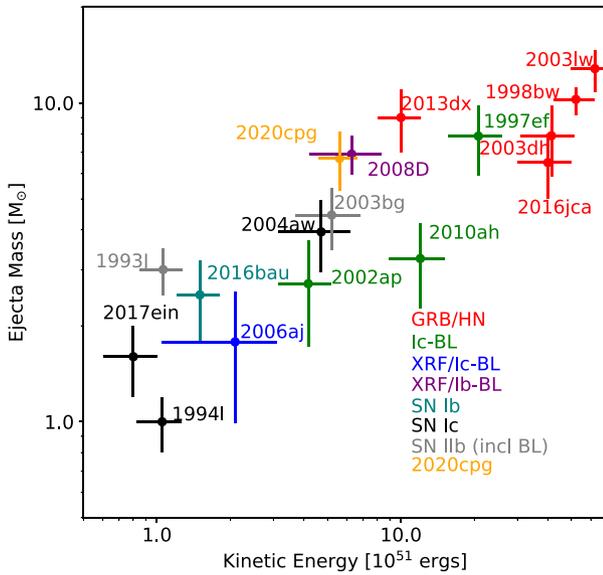| Group	Ib M_{ej} [$M_{\odot}$]	E_k [foe]	M_{Ni} [$M_{\odot}$]
Prentice et al. (2019)	2.2		0.07
Taddia et al. (2018)	3.8 ± 2.1	1.4 ± 0.9	0.14 ± 0.09
Lyman et al. (2016)	2.6 ± 1.1	1.6 ± 0.9	0.17 ± 0.04
Group	IIb M_{ej} [$M_{\odot}$]	– E_k [foe]	– M_{Ni} [$M_{\odot}$]
Prentice et al. (2019)	2.7	–	0.09
Taddia et al. (2018)	4.3 ± 2.0	1.3 ± 0.6	0.15 ± 0.07
Lyman et al. (2016)	1.0 ± 0.6	$1.4 \pm .09$	0.11 ± 0.04

Figure 5. A sample of modelled results from a variety of SN types that show the explosion energy and M_{ej}. SN 2016bau is in prep, but for SN 2016jca see Ashall et al. (2019), for SN 2013dx see Mazzali et al. (2021), for SN 2017ein see Teffs et al. (2021), and for all other remaining SNe see Mazzali et al. (2017) for references.

et al. (2018) estimates M_{ej} values closer to our modelled values but use a lower optical opacity $\kappa = 0.06$–0.07 cm^2 g^{-1} compared to our average opacity of ~ 0.1 cm^2 g^{-1}.

We also compare our modelled parameters to a wider set of SNe of various types that have been modelled using abundance tomography. Figs 5 and 6 show this variety of SNe based upon the three measured values found in this work; M_{Ni}, M_{ej}, and E_k. SN 2008D is nearly coincident with SN 2020cpg in Fig. 5, while having a much lower M_{Ni} as shown in Fig. 6. The broad-lined Type IIb SN 2003bg is also close in parameter space to SN 2020cpg in Fig. 5. The broad-lined nature of the early spectra of SN 2003bg also marks SN 2003bg as an unusual Type IIb.

4.4 Similar SNe

Due to their proximity to SN 2020cpg in Figs 5 and 6 and their status as broad-lined and interesting events, we directly compare SN 2003bg and SN 2008D to SN 2020cpg. The explosion properties for SN 2020cpg result in an E_k/M_{ej} ratio of $0.85^{+0.5}_{-0.3}$ foe $M_{\odot}^{-1}$. Prentice & Mazzali (2017) found a correlation for Type Ic SNe
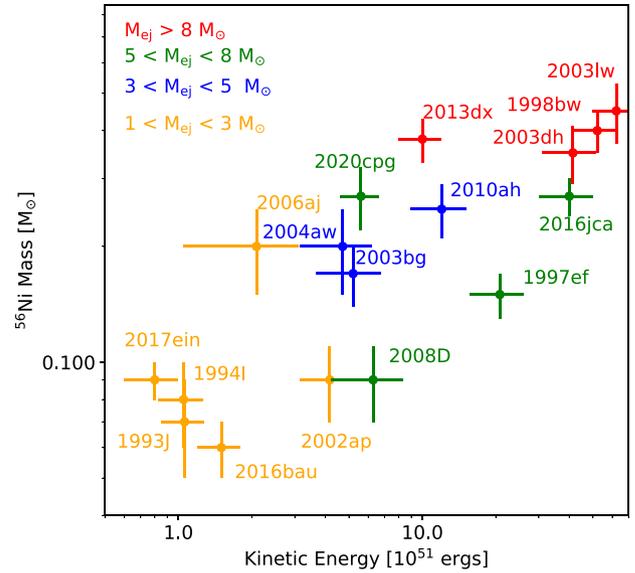

Figure 6. A sample of modelled results with the explosion energy plotted against the M_{Ni}. The SNe are colour coded to match their M_{ej} and see the caption of Fig. 5 for references.

that share a common E_k/M_{ej} value, a similar number of commonly observed spectral features, such as Si II and O I among others, can be identified. As few SNe Type Ib/IIb have been modelled using the abundance tomography method, it is unknown if a similar trend regarding E_k/M_{ej} behaviour holds for SNe Type IIb/Ib.

The explosion properties for SN 2008D (Mazzali et al. 2008) result in an E_k/M_{ej} of ~ 0.85 foe $M_{\odot}^{-1}$, which is approximately identical to that of SN 2020cpg. The explosion properties for the broad-lined Type IIb SN 2003bg (Mazzali et al. 2009) give a higher E_k/M_{ej} ratio of ~ 1.25 foe $M_{\odot}^{-1}$. Under the physical classification system by Prentice & Mazzali (2017), SN 2008D is also as a Type Ib(II), while SN 2003bg keeps its original classification of a Type IIb.

When correcting for reddening, both SN 2008D and SN 2020cpg show comparable spectral shapes with SN 2020cpg showing somewhat shallower features as shown in Fig. 7. The spectral shape and evolution for SN 2003bg is less comparable to that of SN 2008D and SN 2020cpg. One primary difference is the presence of a prominent P-Cygni re-emission feature for Hα as well as the presence of the weaker Balmer series lines that are visible early and in later times. SN 2020cpg has only a weak Hα feature. This may suggest that the H-rich layer in SN 2003bg may be denser or larger than what is in SN 2020cpg or that the ionization found in SN 2020cpg naturally results in weaker H features.

The time evolution of the modelled photospheric velocity for SN 2020cpg and other selected SNe are shown in Fig. 8. SN 2020cpg shows a higher modelled photospheric velocity at similar epochs with respect to the estimated explosion date for SN 2003bg and SN 2008D, and SN 2002ap. We also include the GRB associated SN 2013dx (Mazzali et al. 2021) and SN 2016jca (Ashall et al. 2019) to show that this increased photospheric velocity can be driven by the extremely high energies of these events. SN 2002ap is a broad-lined event (Mazzali et al. 2007) with a relatively low M_{ej} and E_k and shows a similar modelled photospheric velocity evolution to SN 2008D and SN 2003bg.

Table 4 summarizes several properties of a near peak spectrum of SN 2008D, SN 2003bg, and SN 2020cpg. As expected from the estimated M_{Ni}, the modelled L_{ph} for SN 2020cpg is higher than either
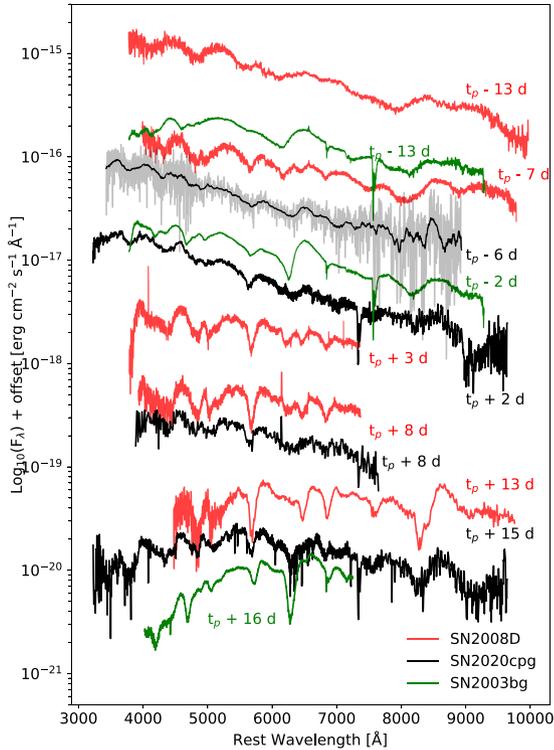
Figure 7. A small sample of SN 2008D, SN 2020cpg, and SN 2003bg spectra at near or similar epochs with respect to $t_{\rm p}$. The first epoch for SN 2020cpg is with a 50 Å boxcar smoothing spectrum overplotted on to the raw, noisy spectrum. We adopt a $z = 0.0065$, $z = 0.037$, and $z = 0.0046$ for SN 2008D, SN 2020cpg, and SN 2003bg, respectively. Each spectrum is reduced to rest frame and corrected for reddening using $E(B-V)_{\rm tot}$ of 0.65 mag for SN 2008D (Mazzali et al. 2008), $E(B-V)_{\rm tot}$ of 0.02 for SN 2003bg (Hamuy et al. 2009; Mazzali et al. 2009), and $E(B-V)_{\rm tot}$ of 0.025 mag for SN 2020cpg (Medler et al. 2021) and the reddening law of Cardelli, Clayton & Mathis (1989).
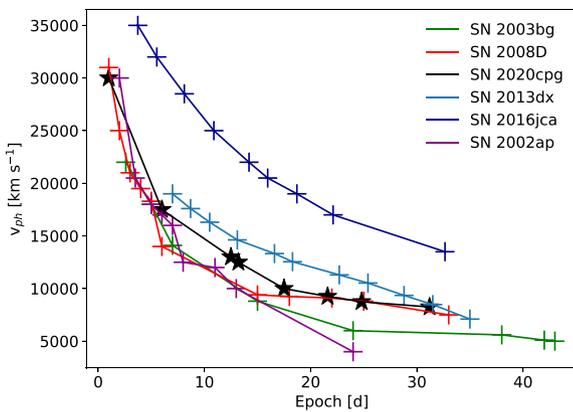

Figure 8. The modelled photospheric velocities as a function of epoch with respect to the estimated $t_{\rm exp}$ as given in Mazzali et al. (2002) for the broad-lined Type Ic SN 2002ap, Mazzali et al. (2009) for Type IIb hypernova SN 2003bg, Mazzali et al. (2008) for broad-lined Type Ib SN 2008D, Ashall et al. (2019) for the GRB associated Type Ic SN 2016jca, and Mazzali et al. (2021) for the GRB associated Type Ic SN 2013dx. The $v_{\rm ph}$ of the first epoch of SN 2020cpg is an estimate as there is no modelled spectrum.

SN 2008D and SN 2003bg. This high luminosity requires a high-photospheric temperature which results in an ionization regime in which the majority of the H/He-rich outer shells are strongly ionized. This ionization regime results in weaker H/He features despite the increased $M_{\rm Ni}$ as compared to SN 2003bg and SN 2008D. The photosphere in the early phases is in the strongly ionized H/He shell, which results in an electron scattering dominated opacity instead of line opacity dominated, which back-scatters more radiation. To counter these effects, the photosphere is moved to higher velocities, and therefore lower densities, which lessens the dominance of the electron scattering opacity. As the photosphere recedes into the CO core at later times, the photospheric velocity flattens and is similar to SN 2008D as the density in the innermost region increases.

Early SNe Type II spectra show a hot, blue continuum with weak features (see Gutiérrez et al. 2017 for a sample of spectra from SNe Type II), as well as some SNe Type IIb such as SN 1993J (Wheeler et al. 1993) and SN 2016gkg (Tartaglia et al. 2017). For H-rich SNe, this behaviour is due to electron scattering dominated H-rich envelopes (Kasen & Bildsten 2010), suggesting the classification of SN 2020cpg leans more towards a Type IIb(I) or Type IIb. The first observed spectrum was observed roughly 10 days after $t_{\rm exp}$, and did not show any easily identifiable features but had a low-S/N ratio. This may suggest that the earliest phases of SN 2020cpg would be given a 'blue, featureless' early classification if observed.

4.5 Progenitor constraints

As discussed before, the lack of nebular phase modelling prevents a strong assessment of the innermost CO-core rich region. Our final model has a total $M_{\rm ej}$ of $\sim(7 \pm 2)\,{\rm M}_\odot$, where $1.08\,{\rm M}_\odot$ of this material is H/He-rich leaving $\sim 5.6\,{\rm M}_\odot$ of CO-rich material. Adopting some remnant mass between 1.4 and $3\,{\rm M}_\odot$, representing a neutron star or low-mass black hole gives us a ~ 7–$9\,{\rm M}_\odot$ CO-core. Comparing this mass to the set of models in Woosley & Heger (2007) gives us a progenitor mass of $M_{\rm ZAMS}$ of 25–30 ${\rm M}_\odot$. For this range of progenitor masses, the estimated mass of the helium shell as defined where the H abundance drops to 20 per cent is ~ 1.2–$1.3\,{\rm M}_\odot$ and a comparable total He core, which is in good agreement with the masses found in this work.

Binary evolution could also be responsible for the stripping observed in our model, but we do not have enough secondary evidence to limit the range of possible companion and orbit parameters. As such, without further evidence, we leave binary companion estimates for future work.

4.6 Nickel disparity

Fig. 6 shows that SN 2003bg, SN 2020cpg, and SN 2008D have a similar final $E_{\rm k}$, but are modelled to have a different ejected $M_{\rm Ni}$. SN 2004aw and SN 2003bg share a similar space in Fig. 5 as well as a similar $M_{\rm Ni}$ in Fig. 6, while this does not hold for SN 2008D and SN 2020cpg. This suggests a few possible scenarios to explain the discrepancy in ejected $M_{\rm Ni}$.

One scenario is that the nucleosynthesis in SN 2020cpg was significantly more efficient than in SN 2008D or that SN 2020cpg has a smaller remnant mass. A large determining factor of explosive nucleosynthesis is the maximum temperature behind the shock, T_s, which Umeda & Nomoto (2008) find that for complete Si shell burning, should be $T_s > 5 \times 10^9$ K. Typically in 1-D simulations as the explosion energy increases, the amount of material that experiences this temperature increases as estimated in Woosley,

Table 4. Properties of modelled spectra at or near t_p for SN 2003bg, SN 2020cpg, and SN 2008D given by private communication with the author. For the missing values of SN 2008D, the data from the original authors is unavailable.

SN	$\log(L_{ph})$ -	v_{ph} [km s^{-1}]	T_E [K]	X (H)	Electron density [10^{10} cm^{-3}]	Epoch [d]
SN2020cpg	42.69	10 000	10191	0	0.992	17.5
SN2008D	42.2	9250	–	–	–	15–20
SN2003bg	42.31	8800	7786	0.13	0.483	15

Heger & Weaver (2002) as $R_{Ni} \sim 3700\, E_{51}^{*1/3}$ km, where E^* is defined as $E^* = 4\pi R_{51}^3 aT_s^4/3$, with $T_s = 5 \times 10^9$ K (e.g. Thielemann, Nomoto & Hashimoto 1996). As the explosion energy for both SN 2008D and SN 2020cpg are similar, the radius of explosive Si-burning and ideally the shock temperature should be the same. Umeda & Nomoto (2008) finds that for a progenitor mass of $\sim 30\,M_\odot$ and a 1 foe explosion, the upper limit of ^{56}Ni production during core collapse is $0.69\,M_\odot$. For a more energetic 10 foe explosion, the upper limit increases to $1.43\,M_\odot$ with both upper limits assuming an inner mass cut-off just above the Fe core. These models also retain an O-rich ejecta mass of 5.45 and $4.65\,M_\odot$, respectively, which is similar to our remaining CO-rich material. This could suggest that SN 2008D had more mass fallback on to the remnant, leading to a reduced total ^{56}Ni or that SN 2020cpg ejected more material with less fallback. However, with no nebular spectra available for SN 2020cpg, a detailed physical explanation is unavailable.

A second scenario is that the peak luminosity in SN 2020cpg is not entirely driven by the decay chain of ^{56}Ni, and therefore the total M_{Ni} is overestimated. A secondary energy source, such as the deposition of energy from a magnetar spin-down phase (e.g. Kasen & Bildsten 2010) could be responsible for some fraction of the total luminosity. Afsariardchi et al. (2021) estimate that the M_{Ni} distribution calculated from Arnett's rule in a sample of SNe can be overestimated and 7–50 per cent of the peak luminosity could be from secondary energy sources. If this is the case for SN 2020cpg, then the M_{Ni} as derived from the peak luminosity is overestimated, and shows no discrepancy in total M_{Ni}. A comparable M_{Ni} is found for SN 2020cpg from the fitting of the tail using the method in Afsariardchi et al. (2021). No nebular spectra were taken of SN 2020cpg, which would allow for a third measurement of the ^{56}Ni mass. For SN 2008D, Afsariardchi et al. (2021) find similar ^{56}Ni masses using the peak L_{Bol}, and from fitting the radioactive tail and the nebular phase of SN 2008D did match the previously estimated M_{Ni} from spectral analysis (Tanaka et al. 2009). We also have no additional information that would suggest the presence of magnetar energy deposition as the ^{56}Ni dominant light curve calculated in Fig. 3 matches the observed bolometric light curve and an Arnett-like fit by Medler et al. (2021) also reproduces the light-curve behaviour.

A final scenario is that the discrepancy is due to a failed GRB that drastically increased the extent of the ^{56}Ni forming region by depositing the majority of its energy into the innermost layers rather than breaking through the surface (e.g. Piran et al. 2019). This increased deposition of energy beyond the initial collapse may increase the size of the ^{56}Ni forming region further into the Si-rich shell, and thus result in an increase in synthesized ^{56}Ni. An X-ray flash was associated with SN 2008D, which was also thought to contain a GRB. The early broad phases of SN 2008D are due to the high-velocity material ejected from the off-angle GRB jet. While Medler et al. (2021) suggest SN 2020cpg shows a high-velocity Hα line formed from high-velocity material, we can reproduce the feature in the spectral evolution without the need of a detached H shell.

For SN 2020cpg, we also do not have any γ- or X-ray detections coincident with the location of SN 2020cpg. With no nebular phase spectra, we are also unable to determine if there is any evidence of asymmetry in the nebular line profiles, which may further suggest GRB formation.

5 CONCLUSIONS

Using the abundance tomography method, a best-fitting model for SN 2020cpg is found that has an M_{ej} of $\sim(7 \pm 2)\,M_\odot$, a final explosion energy of $\sim(6 \pm 1) \times 10^{51}$ erg, and a M_{Ni} of $0.27 \pm 0.05\,M_\odot$. This model has $0.08\,M_\odot$ of hydrogen and $\sim 1.0\,M_\odot$ of helium above a CO-rich ejecta of $\sim 5\,M_\odot$. Using these parameters, SN 2020cpg has an $E_k/M_{ej} = 0.85^{+0.5}_{-0.3}$ foe $M_\odot^{-1}$. This model reproduces both the light curve and the observed spectral evolution. The Hα region near 6500 Å in this model does not require a detached shell with high-velocity Hα in order to reproduce the early and late time spectra. Throughout the evolution, this feature is comprised of C II, Si II, Hα, and He I in the earliest phases before becoming dominated by Si II, Hα, and He I in the final modelled epochs. Removing H from the model results in a worse fit to the Hα region with a split feature dominated by Si II, C II, and He I.

The lack of strong re-emission from Hα favours a Type Ib classification and additionally, the spectra of SN 2020cpg only shows a weak Hα feature and no other Balmer series lines. The similarity with SN 2008D also favours the Type Ib classification. The Hα spectral region is best fit with hydrogen present in the model which favours a Type IIb instead, so we identify SN 2020cpg to be an unusual, luminous transient that best fits between a Type IIb and a Type Ib. Using the physical classification of Prentice & Mazzali (2017), SN 2020cpg is also a transitional SN as it fits between a Type IIb (I) and a Type Ib (II) classifications due to the lack of strong re-emission and a poorly defined equivalent width.

Comparing the explosion properties from SN 2020cpg to a set of synthetic stellar evolution models, and assuming a remnant mass of 1.5–3 $M_\odot$, a progenitor mass of 25–30 $M_\odot$ that is stripped of most of its hydrogen and some of its helium prior to collapse matches our modelled values for the CO-rich ejecta and the total remaining H/He mass.

There is a continued trend in the M_{ej}/E_k space from other SNe modelled using the abundance tomography method. SN 2020cpg has a higher M_{Ni} as compared to other SNe of a similar mass range, but similar to those of a comparable explosion energy. This suggests that the nucleosynthesis in SN 2020cpg was more efficient for its mass or that less material fell back during the initial explosion, resulting in an increase in ejected ^{56}Ni mass. The nucleosynthesis may also have enhanced by a GRB jet that failed to break the surface and deposited energy into the ^{56}Ni forming region. An alternative explanation is that the M_{Ni} may be overestimated and a secondary energy source such as a magnetar may contributed to the high L_{Bol}, but there is no additional evidence to suggest this as a likely scenario.

After correcting for extinction, SN 2020cpg shows similar spectral behaviours to SN 2008D. This implies SN of a similar E_k/M_{ej} show similar spectral shapes and behaviours.

DATA AVAILABILITY

Model data can be shared on reasonable request to the corresponding author.

REFERENCES

Afsariardchi N., Drout M. R., Khatami D. K., Matzner C. D., Moon D.-S., Ni Y. Q., 2021, ApJ, 918, 89
Amenouche M., Möller A., Smith M., Pursiainen M., Müller T., Angus C., Yaron O., 2020, TNS Class. Rep., 2020-1498, 1
Arnett W. D., 1982, ApJ, 253, 785
Ashall C., Mazzali P. A., 2020, MNRAS, 492, 5956
Ashall C., Mazzali P. A., Pian E., James P. A., 2016, MNRAS, 463, 1891
Ashall C. et al., 2019, MNRAS, 487, 5824
Axelrod T. S., 1980, PhD thesis, California Univ., Santa Cruz
Cappellaro E., Mazzali P. A., Benetti S., Danziger I. J., Turatto M., della Valle M., Patat F., 1997, A&A, 328, 203
Cardelli J. A., Clayton G. C., Mathis J. S., 1989, ApJ, 345, 245
Gutiérrez C. P. et al., 2017, ApJ, 850, 89
Hachinger S., Mazzali P. A., Taubenberger S., Pakmor R., Hillebrandt W., 2009, MNRAS, 399, 1238
Hachinger S., Mazzali P. A., Taubenberger S., Hillebrandt W., Nomoto K., Sauer D. N., 2012a, MNRAS, 422, 70
Hachinger S., Mazzali P. A., Taubenberger S., Fink M., Pakmor R., Hillebrandt W., Seitenzahl I. R., 2012b, MNRAS, 427, 2057
Hamuy M. et al., 2009, ApJ, 703, 1612
Harkness R. P. et al., 1987, ApJ, 317, 355
Kasen D., Bildsten L., 2010, ApJ, 717, 245
Langer N., 2012, ARA&A, 50, 107
Lucy L. B., 1999, A&A, 345, 211
Lyman J. D., Bersier D., James P. A., Mazzali P. A., Eldridge J. J., Fraser M., Pian E., 2016, MNRAS, 457, 328
Mazzali P. A., 2000, A&A, 363, 705
Mazzali P. A., Lucy L. B., 1993, A&A, 279, 447
Mazzali P. A., Nomoto K., Cappellaro E., Nakamura T., Umeda H., Iwamoto K., 2001, ApJ, 547, 988
Mazzali P. A. et al., 2002, ApJ, 572, L61
Mazzali P. A. et al., 2006, ApJ, 645, 1323
Mazzali P. A. et al., 2007, ApJ, 670, 592
Mazzali P. A. et al., 2008, Science, 321, 1185
Mazzali P. A., Deng J., Hamuy M., Nomoto K., 2009, ApJ, 703, 1624
Mazzali P. A., Walker E. S., Pian E., Tanaka M., Corsi A., Hattori T., Gal-Yam A., 2013, MNRAS, 432, 2463
Mazzali P. A. et al., 2015, MNRAS, 450, 2631
Mazzali P. A., Sauer D. N., Pian E., Deng J., Prentice S., Ben Ami S., Taubenberger S., Nomoto K., 2017, MNRAS, 469, 2498
Mazzali P. A., Pian E., Bufano F., Ashall C., 2021, MNRAS, 505, 4106
Medler K. et al., 2021, MNRAS, 506, 1832
Nomoto K., Iwamoto K., Suzuki T., 1995, Physics Reports, 256, 173
Nordin J., Brinnel V., Giomi M., Santen J. V., Gal-Yam A., Yaron O., Schulze S., 2020, TNS Discovery Report, 2020-511, 1
Piran T., Nakar E., Mazzali P., Pian E., 2019, ApJ, 871, L25
Poidevin F. et al., 2020, TNS Classification Report, 2020-571, 1
Prentice S. J., Mazzali P. A., 2017, MNRAS, 469, 2672
Prentice S. J. et al., 2016, MNRAS, 458, 2973
Prentice S. J. et al., 2019, MNRAS, 485, 1559
Sauer D. N., Mazzali P. A., Deng J., Valenti S., Nomoto K., Filippenko A. V., 2006, MNRAS, 369, 1939
Stehle M., Mazzali P. A., Benetti S., Hillebrandt W., 2005, MNRAS, 360, 1231
Stritzinger M. et al., 2009, ApJ, 696, 713
Taddia F. et al., 2018, A&A, 609, A136
Tanaka M. et al., 2009, ApJ, 700, 1680
Tartaglia L. et al., 2017, ApJ, 836, L12
Taubenberger S. et al., 2011, MNRAS, 413, 2140
Teffs J., Ertl T., Mazzali P., Hachinger S., Janka H. T., 2020, MNRAS, 499, 730
Teffs J. J., Prentice S. J., Mazzali P. A., Ashall C., 2021, MNRAS, 502, 3829
Thielemann F.-K., Nomoto K., Hashimoto M.-A., 1996, ApJ, 460, 408
Umeda H., Nomoto K., 2008, ApJ, 673, 1014
Wheeler J. C. et al., 1993, ApJ, 417, L71
Woosley S. E., Heger A., 2007, Phys. Rep., 442, 269
Woosley S. E., Heger A., Weaver T. A., 2002, Rev. Mod. Phys., 74, 1015
Yoon S.-C., Woosley S. E., Langer N., 2010, ApJ, 725, 940

This paper has been typeset from a TEX/LATEX file prepared by the author.